

Molecular dissolution behaviors on porous membrane surface using hierarchical metal-organic framework lamellar membrane

Yihao Chen¹, Jingjing Chen², Chongchong Chen², Xiaoli Wu¹, Yifan Li², Jie Zhang², and jingtao wang²

¹Affiliation not available

²Zhengzhou University

September 22, 2022

Abstract

Lamellar membranes, especially assembled by microporous framework nanosheets, have excited interest for fast molecular permeation. However, the underlying molecular dissolution behaviors on membrane surface, especially at pore entrances, remain unclear. Here, hierarchical metal-organic framework (MOF) lamellar membranes with 7 nm-thick surface layer and 553 nm-thick support layer are prepared. Hydrophilic ($-\text{NH}_2$) or hydrophobic ($-\text{CH}_3$) groups are decorated at pore entrances on surface layer to manipulate wettability, while $-\text{CH}_3$ groups on support layer provide comparable, low-resistance paths. We demonstrate that molecular dissolution behaviors are determined by molecule-molecule and molecule-pore interactions, derived from intrinsic parameters of molecule and membrane. Importantly, two dissolution model equations are established: for hydrophobic membrane surface, dissolution activation energy (E_S) obeys $E_S = K_m \ln[(\gamma_L - \gamma_C) \mu d^2]$, while turns to $E_S = K_m \ln[(\gamma_L - \gamma_C) \delta \mu d^2]$ for hydrophilic one. Particularly, hydrophilic pore entrances exert strong interaction with polar molecules, thus compensating the energy consumed by molecule rearrangement, giving fast permeation ($> 270 \text{ L m}^{-2} \text{ h}^{-1} \text{ bar}^{-1}$).

Molecular dissolution behaviors on porous membrane surface using hierarchical metal-organic framework lamellar membrane

Yihao Chen⁺, Jingjing Chen⁺, Chongchong Chen⁺, Xiaoli Wu^{*,++}, Yifan Li⁺, Jie Zhang⁺, Jingtao Wang^{*,+,++}

⁺School of Chemical Engineering, Zhengzhou University, Zhengzhou 450001, P. R. China.

⁺⁺Henan Institute of Advanced Technology, Zhengzhou University, Zhengzhou 450003, P. R. China.

E-mails: jingtaowang@zzu.edu.cn (J. Wang); xiaoliwu@zzu.edu.cn (X. Wu)

Abstract

Lamellar membranes, especially assembled by microporous framework nanosheets, have excited interest for fast molecular permeation. However, the underlying molecular dissolution behaviors on membrane surface, especially at pore entrances, remain unclear. Here, hierarchical metal-organic framework (MOF) lamellar membranes with 7 nm-thick surface layer and 553 nm-thick support layer are prepared. Hydrophilic ($-\text{NH}_2$) or hydrophobic ($-\text{CH}_3$) groups are decorated at pore entrances on surface layer to manipulate wettability, while $-\text{CH}_3$ groups on support layer provide comparable, low-resistance paths. We demonstrate that molecular dissolution behaviors are determined by molecule-molecule and molecule-pore interactions, derived from intrinsic parameters of molecule and membrane. Importantly, two dissolution model equations are established: for hydrophobic membrane surface, dissolution activation energy (E_S) obeys $E_S = K_m \ln[(\gamma_L - \gamma_C) \mu d^2]$

$c)\mu\delta^2]$, while turns to $E_s = K_a \ln[(\gamma_L - \gamma_C)\delta_e \mu \delta^2]$ for hydrophilic one. Particularly, hydrophilic pore entrances exert strong interaction with polar molecules, thus compensating the energy consumed by molecule rearrangement, giving fast permeation ($> 270 \text{ L m}^{-2} \text{ h}^{-1} \text{ bar}^{-1}$).

KEYWORDS

metal-organic framework, hierarchical lamellar membrane, pore entrance, dissolution activation energy, dissolution model equation

1 INTRODUCTION

Membrane separation technology with high energy efficiency and low carbon footprints has drawn increasing attention in a wide range of applications including petroleum refining, water purification and carbon capture, *etc.*^[1-5] Two-dimensional (2D) lamellar membranes with controllable microstructure and well-aligned nanochannels make excellent candidates for devising fast molecule permeation and precise sieving.^[6-8] Typically, membranes assembled by porous nanosheets offer continuous transfer highways in vertical direction, which further shortens mass transfer distance and permits fast transport.^[9-11] Molecule transport through porous lamellar membranes should firstly dissolve into pore entrances on membrane surface and then diffuse through inner pores. It has been demonstrated that the resistance of molecular dissolution process accounts for 20% ~ 40% of the total transport resistance, and even 70% for membranes with sub-10 nm thickness.^[12-14] Therefore, molecular dissolution process exerts huge and even decisive impact on molecular transport efficiency, which deserves the investigation of underlying molecular dissolution behaviors on membrane surface.

In general, experimental researches have confirmed that enhancing the affinity of membrane surface to molecules by grafting active sites or attaching compatible films could obviously improve molecular dissolution rate and hence permeation ability.^[15-17] As a noteworthy example, water-capture capacity of over 300% was achieved for graphene oxide (GO) lamellar membrane by modifying tannic acid on membrane surface, which highly improve water permeance from 175 to 320 $\text{L m}^{-2} \text{ h}^{-1}$.^[18] These observations are generally attributed to the strong molecule-membrane interactions that enrich molecules on membrane surface and promote them to enter into inner channels. In contrast, recent studies discovered that due to the strong interactions between water molecules and $-\text{COO}^-$ groups on the pore rim of aquaporins, water permeance was 6 times lower than in carbon nanotube porins (CNTPs) which possessed similar channel size but hydrophobic pore rim.^[19] This phenomenon parallels findings by simulation where the addition of four $-\text{COO}^-$ groups to the rims of a 1.1-nm-diameter CNTPs reduced the water flux by 3 folds due to the enhanced water-rim interactions. These controversial viewpoints suggest that molecular dissolution behaviors need deep investigation, especially for porous materials. On the other hand, expect for molecule-membrane interaction, other factors such as molecule-molecule interaction should also count much due to the confinement effect of molecules on pore entrances. However, the pores in current porous lamellar membrane are usually artificially created with random distribution and wide pore size distribution.^[20-22] And the chemical groups on pore entrances are heterogeneous, which hampers the control of molecule-pore interactions on molecule level. More importantly, lamellar membranes generally possess homogeneous structure, and the high resistance of molecular diffusion in inner pores exerts huge impact on molecule permeance. This conceals the contribution of dissolution process on molecule permeance, hence impeding the exploration of underlying molecular dissolution behaviors.^[20,23,24] Therefore, constructing hierarchical porous lamellar membranes with independently manipulated surface and support layers, and especially regular and controllable pore entrances on surface layer, should provide desired platform.

Metal-organic frameworks (MOFs) show great expectations as next-generation materials for porous membranes because of intrinsic characteristics including large porosity, well-defined pore structures, and tunable molecule-/ion- specific functional groups.^[25-29] Significantly, the intrinsic pores (usually $< 2 \text{ nm}$) in MOF nanosheets can be subtly tailored by controlling metallic node and organic linkers.^[30-32] And the topology and chemical composition of pores are periodically distributed within the frameworks, which permits subtle manipulation of molecule-pore interaction on molecule level. Additionally, some MOFs can be synthesized

in the form of ultrathin nanosheets with large lateral size ($> 2 \mu\text{m}$), holding promise for constructing porous lamellar membranes.^[9,33,34] On the other hand, electrostatic atomization technology provides a novel strategy to evenly spray atomized nanodrops that carry desired nanosheets onto receiver to assemble ultrathin lamellar architectures.^[35,36] In this way, hierarchical lamellar membranes with independently controlled surface and support layer can be facilely constructed.

Herein, hierarchical MOF lamellar membranes with ultrathin ($\sim 7 \text{ nm}$) surface layer and identical support layer ($\sim 553 \text{ nm}$) were prepared *via* double-needled electrostatic atomization technology. Specifically, MOF nanosheets with hydrophobic ($-\text{CH}_3$) pores were sprayed on Nylon substrate to construct support layers. And MOF nanosheets with hydrophilic ($-\text{NH}_2$) or hydrophobic ($-\text{CH}_3$) groups on pores were assembled to create surface layers, respectively. Based on these platforms, molecular dissolution behaviors on porous membrane surface was investigated in detail. Dissolution performances demonstrate that molecular dissolution behaviors are highly affected by molecule-molecule and molecule-pore interactions. Furthermore, the corresponding dissolution model equations were established in term of dissolution activation energy (E_s) on membrane surface with hydrophilic and hydrophobic pore entrances. Importantly, membrane with hydrophilic pores on surface exerts strong interactions with polar solvents, contributing to low E_s and high permeance of over $270 \text{ L m}^{-2} \text{ h}^{-1} \text{ bar}^{-1}$ for polar solvents. In addition, the regular pores within MOF lamellar membranes bring precise sieving with rejection of 99% for reactive red ($1.6 \times 1.4 \text{ nm}$). The elucidation of molecular dissolution behaviors on membrane surface is paramount to develop highly permeable and selective membranes for separation applications.

2 MATERIALS AND METHODS

2.1 Materials

$\text{NiCl}_2 \cdot 6\text{H}_2\text{O}$ (99.9%) and $\text{CoCl}_2 \cdot 6\text{H}_2\text{O}$ (99.9%) were purchased from Aladdin Reagent. Triethylamine (TEA), benzenedicarboxylic acid (BDC), 2-aminoterephthalic acid ($\text{NH}_2\text{-BDC}$), 2-methylterephthalic acid ($\text{CH}_3\text{-BDC}$) and diiodomethane were bought from Macklin Reagent. Organic solvents (methanol, ethanol, dimethyl sulfoxide (DMSO), N,N-dimethylformamide (DMF), acetonitrile, acetone, n-octane, cyclohexane, n-hexane, n-pentane and toluene) were obtained from Tianjin Kemiou Chemistry Reagent Co., Ltd. Nylon micro-filtration substrates ($0.2 \mu\text{m}$ pore size, 50 mm diameter) were bought from Tianjin Jinteng Experimental Equipment Co., Ltd. Polyethylene glycol (PEG, 200, 300, 400, 600, 800, 1000), Brilliant blue (BB), reactive red (RR), rhodamine B (RB), crystal violet (CV), and methylene blue (MB) were supplied by Aladdin Chemical Co., Ltd. These were used as received without further treatment, and deionized water was used throughout the experiment.

2.2 Synthesis of MOF nanosheets

The MOF nanosheets were solvothermally synthesized under continuous ultrasonication as reported in literature.^[37] Primarily, 0.375 mmol $\text{CoCl}_2 \cdot 6\text{H}_2\text{O}$ and 0.375 mmol $\text{NiCl}_2 \cdot 6\text{H}_2\text{O}$ were fully dissolved in 32 mL DMF. Then, ethanol (2 mL), water (2 mL), and TEA (0.8 mL) were added into the solution under constant stirring, followed by adding 0.375 mmol organic ligands (BDC, $\text{NH}_2\text{-BDC}$, or $\text{CH}_3\text{-BDC}$). The organic ligands were completely dissolved in solution and it was further stirred for 2 h to obtain a uniform colloidal suspension. Whereafter, the colloidal suspension was continuously ultrasonicated for 20 h under airtight condition and the precipitates were collected *via* centrifugation. The obtained MOF nanosheets were then washed with ethanol by 4 times to remove the residual reactants, and vacuum dried at room temperature. Finally, MOF nanosheets were dispersed in ethanol for further utilization.

2.3 Preparation of hierarchical MOF lamellar membranes

Hierarchical MOF lamellar membranes were prepared by double-needled electrostatic atomization technology as shown in Scheme 1. Primarily, Nylon substrates were smoothly adhered on the receiver roller. MOF- CH_3 nanosheet dispersion (0.1 g L^{-1}) was injected into one syringe (A), and MOF- CH_3 , MOF-BDC or MOF- NH_2 nanosheet dispersion (0.1 g L^{-1}) was injected into another syringe (B). The two syringes both connected with a high voltage of 18 kV , and the tip-to-collector distance was 15 cm . Subsequently, 240 mL MOF- CH_3

nanosheet dispersion in A syringe was pumped out at a speed of 0.005 mm s⁻¹ along with scanning cyclically along roller surface at a speed of 160 rpm to prepare support layer. After that, 3 mL solution in B syringe was sprayed on the support layer under the same conditions, to construct ultrathin membrane surface layer.

Hosted file

image1.emf available at <https://authorea.com/users/510119/articles/587306-molecular-dissolution-behaviors-on-porous-membrane-surface-using-hierarchical-metal-organic-framework-lamellar-membrane>

Scheme 1. Schematic illustration of the hierarchical MOF lamellar membrane preparation.

2.4 Characterization of nanosheets and lamellar membranes

The structure and morphology of MOF nanosheets and hierarchical MOF lamellar membranes were characterized by X-ray diffraction (XRD, RigakuD/max2500 v/Pc), N₂ absorption and desorption (Quantachrome Ltd., America), atomic force microscopy (AFM, Bruker Dimension FastScan), scanning electron microscope (SEM, Auriga FIB SEM, Zeiss, Germany), and high-resolution transmission electron microscopy (HRTEM, Tecnai G2 F20, FEI, U.S.). The chemical properties were analyzed by X-ray photoelectron spectroscopy (XPS, AXIS Supra, Kratos, UK) and fourier transform infrared spectroscopy (FTIR, Nicolet MANGNA-IR560). The wettability and dynamic contact angle were probed by FACE (model OCA 25, Germany).

2.5 Nanofiltration performance of hierarchical MOF lamellar membranes

Nanofiltration performance was evaluated after immersing hierarchical MOF lamellar membrane in corresponding solution for 3 h to reach a fully equilibrium state. Based on the home-made device, solvent permeance and dye rejection were tested. Dyes dissolved in methanol (10 mg L⁻¹) were used for rejection measurement and analyzed by UV-vis spectrophotometer. The solvent permeance P (L m⁻² h⁻¹ bar⁻¹) was calculated by using the following equation:

$$P = \frac{V}{P \times A \times t} \quad (1)$$

where V , $\Delta\Pi$, A and t , represent the permeate volume (L), operating pressure (bar), effective membrane area (m²), and testing time (h), respectively. The following expression was obtained for the calculation of dye rejection (R , %):

$$R = \left(1 - \frac{C_p}{C_f}\right) \times 100 \quad (2)$$

where C_f and C_p are the concentration of feed solution and permeate solution, respectively. The obtained data were average of three parallel tests.

3 RESULTS AND DISCUSSION

3.1 Preparation and characterization of hierarchical MOF lamellar membranes

MOF nanosheets were solvothermally synthesized from a mixed solution of metal ions (Ni²⁺, Co²⁺) and organic linkers under continuous ultrasonication.^[37] Here, three kinds of organic linkers with distinct functional groups (-CH₃, -NH₂, and no extra groups) were selected (Figure S1), which are designed to construct MOF nanosheets bearing intrinsic pores with close size but different groups. These nanosheets were denoted as MOF-CH₃, MOF-NH₂, and MOF-BDC, corresponding to the constructed organic ligands, respectively. AFM and SEM images in Figure 1a and Figures S2, S3 show that the synthesized MOF samples display typical sheet morphology, with uniform transverse size of ~ 1.5 μm and thickness of ~ 3.7 nm. And the XRD spectra (Figure 1b) show that three MOF nanosheets possess the same lattice structure, where the typical (200) peak at $2\theta = 8.7^\circ$ reflects the intrinsic pores.^[37] This agrees with the HRTEM images in Figure S4, which visually show the lattice spacing of ~ 1.05 nm for these nanosheets.^[38,39] Furthermore, N₂ sorption/desorption spectra, Figures 1c and S5, reveal that the average pore sizes for MOF-CH₃, MOF-NH₂ and MOF-BDC nanosheets are 1.12 nm, 1.05 nm, and 1.29 nm, respectively. It should be noted that the pore size of MOF-CH₃

and MOF-NH₂ nanosheets is smaller than that of MOF-BDC nanosheet, which is originated from the steric effect of -CH₃ and -NH₂ groups on the pores.^[40,41]

FTIR result (Figure S6) shows that, compared with MOF-BDC nanosheet, the typical C=O peak gives a blue shift for MOF-CH₃ and MOF-NH₂ nanosheets at 1360 ~ 1380 cm⁻¹, owing to the presence of -CH₃/-NH₂ groups adjacent to C=O group. Meanwhile, the grafting of -NH₂ groups bring a new strong peak at 1253 cm⁻¹, which assigned to Ar-N on FTIR and a typical characteristic peak of N element at 400 eV in XPS spectra of MOF-NH₂ (Figure S7).^[42] While the decorating of -CH₃ groups is supported by the higher C element content for MOF-CH₃ relative to MOF-BDC. Specifically, the content of N element on MOF-NH₂ nanosheet is tested to be 2.95%, matching well with the theoretical value calculated from lattice structure. This also implies that there is one -NH₂ group in a unit cell,^[41] and the condition is identical for MOF-CH₃ nanosheet (Figures 1g and i), this implies the topological structure of MOF is explicitly constructed during synthetic process. Note that there is no extra group in the pore of MOF-BDC nanosheet, which is designed as a comparison.

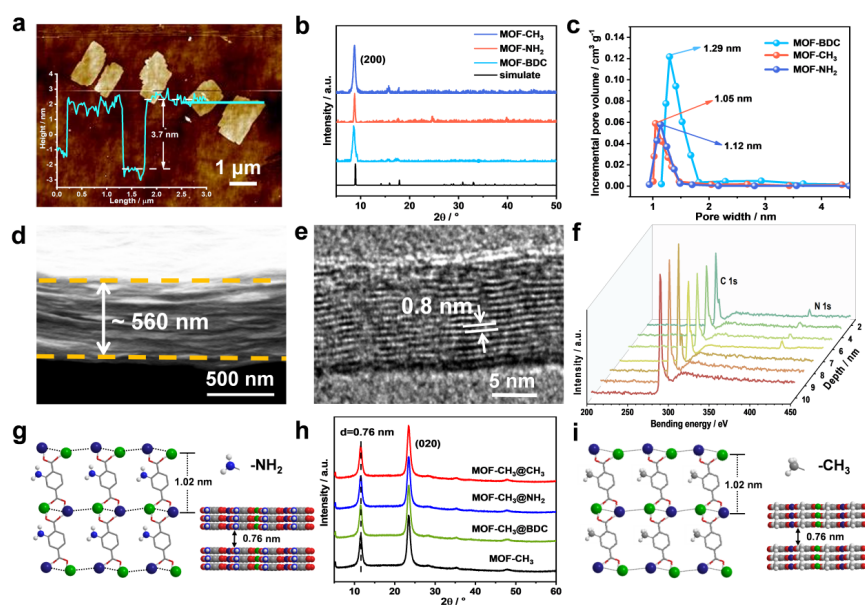


Figure 1. Characterization of MOF nanosheets and membranes. (a) AFM image of MOF-CH₃ nanosheets. (b) XRD patterns and (c) pore size distributions of MOF-BDC, MOF-CH₃ and MOF-NH₂ nanosheets. Cross-sectional (d) SEM and (e) HRTEM images of MOF-CH₃@NH₂ membrane. (f) XPS depth profiles of MOF-CH₃@NH₂ membrane. Models of the pore structure (left) and the stacking configuration of nanosheets (right) for (g) MOF-CH₃@NH₂ and (i) MOF-CH₃@CH₃ membrane surfaces, corresponding to XRD data. (h) XRD patterns of hierarchical MOF lamellar membranes.

Next, hierarchical MOF lamellar membranes were prepared by double-needled electrostatic atomization technology. Concretely, MOF-CH₃ nanosheets were sprayed on Nylon substrate to construct a smooth support layer, and the hydrophobic micropores of which would provide low-resistance diffusion paths for molecules that dissolve through the surface layer.^[19] Subsequently, MOF nanosheets (MOF-CH₃, MOF-BDC or MOF-NH₂) were sprayed on support layer to assemble surface layer. The strong electrostatic repulsion among nanosheets under high-voltage field, coupled with the shear force from rotational receiver, contribute to flat deposition of MOF nanosheets on substrate (Scheme 1).^[43] The obtained hierarchical lamellar membranes were marked as MOF-CH₃@CH₃, MOF-CH₃@BDC and MOF-CH₃@NH₂ membranes, respectively.

AFM and SEM images in Figures S8 and S9 show that membrane surface is defect-free and smooth, in-

dicating the ordered stacking of MOF nanosheets. This can be directly confirmed by the cross-sectional SEM and HRTEM images in Figures 1d, e and Figures S10, S11, which also deliver the information that the interlayer space is ~ 0.8 nm and the membrane thickness is around 560 nm. Here, it should be noted that, considering the nanofiltration performance and mechanical stability, membrane thickness of 560 nm is selected. Additionally, the ordered stacking of MOF nanosheets is further identified by the sharp peaks at $2\theta = 11.4^\circ$ on XRD spectra of membranes, which also suggests the interlayer space of 0.76 nm (Figure 1h). And the corresponding structural models are presented in Figures 1g and i.^[38] It should be noted that the typical (200) peak for MOF powder is not observed in the spectra of MOF membrane, it is ascribed to the strong diffraction peaks corresponding to nanosheet stacking could mask the weak peaks of MOF powder. This phenomenon is also reported in other literature.^[44] Here, MOF-CH₃@CH₃, MOF-CH₃@BDC and MOF-CH₃@NH₂ membranes are prepared with similar thickness (~ 560 nm) for the following performance testing. Next, MOF-CH₃@NH₂ membranes are employed to XPS compositional depth analysis (Figures 1f and S13b), which shows that the peak of N element (400 eV) disappears abruptly and that of C element (285 eV) enhances at ~ 7 nm. This observation validates that the MOF lamellar membrane contains hierarchical structure, and the thickness of surface layer is around 7 nm. The results are similar for MOF-CH₃@BDC membranes as shown in Figures S12 and S13. Furthermore, the manipulated surface layer endows MOF lamellar membranes with distinct wettability. As shown in Figure S14, water contact angles are 38.1°, 71.3°, and 100.6° for MOF-CH₃@NH₂, MOF-CH₃@BDC, and MOF-CH₃@CH₃ membranes, respectively, indicating the hydrophilicity of MOF-CH₃@NH₂ and hydrophobicity of MOF-CH₃@CH₃ membrane surfaces. Such ultrathin and adjustable surface layers with regular pores should provide suitable platform for the investigation of molecular dissolution behaviors.

3.2 Solvent permeance of hierarchical MOF lamellar membranes

The solvent permeance of hierarchical MOF lamellar membranes was evaluated by a home-made dead-end cell under pressure of 1.0 bar using seven polar solvents and five nonpolar solvents (Figure S15). Results in Figure 2 reveal that hierarchical MOF lamellar membranes permit fast molecule transport: 275.4 and 266.8 L m⁻² h⁻¹bar⁻¹ for acetone and n-pentane, respectively. The permeance is almost one order of magnitude higher than that of nonporous graphene-based membranes (Figure S16). This is contributed by the vertical channels throughout the membrane architecture, which greatly shorten mass transfer distance and reduce transfer resistance.^[21,22] Furthermore, Figure 2a shows that the permeance displays a good linear relationship with reciprocal of solvent viscosity for MOF-CH₃@BDC membrane, that is, obeying Hagen-Poiseuille equation.^[45] While for MOF-CH₃@CH₃ and MOF-CH₃@NH₂ membranes (Figures 2b and c), molecule transport deviates obviously from Hagen-Poiseuille law, implying that it is also affected by other factors expect for viscosity, *e.g.* molecular diameter and solubility parameter.^[46] In general, the permeance of polar solvents is higher than that of nonpolar solvents for MOF-CH₃@NH₂ membrane, while the condition is inverse for MOF-CH₃@CH₃ membrane. Taking acetone and n-hexane with similar viscosity as examples, MOF-CH₃@NH₂ membrane gives a permeance of 275.4 L m⁻² h⁻¹bar⁻¹ for acetone, which is about 2 times higher than that of n-hexane. While for MOF-CH₃@CH₃ membrane, acetone permeance is 119.1 L m⁻² h⁻¹ bar⁻¹, about half of that of n-hexane permeance (214.8 L m⁻²h⁻¹ bar⁻¹). Since these hierarchical lamellar membranes bear identical support layer, the variation of molecule permeance should derive from distinct dissolution efficiency on surface layer. Water and diiodomethane contact angles on the membrane surfaces (Figure S17) show that water contact angle on hydrophilic surface of MOF-CH₃@NH₂ membrane decreases quickly in the first 1 s. And then it continues to drop moderately, confirming the positive tendency for water molecules drilling into the subcutaneous tissue of membrane surface. In contrast, hydrophobic MOF-CH₃@CH₃ membrane surface permits diiodomethane to spread more smoothly than water, proving the strong affinity toward nonpolar molecules. However, the contact angles keep almost constant after initial spreading, which implies that hydrophobic pores give inert dissolution to both polar and nonpolar solvents.^[47] These observations deliver the fact that molecular dissolution behavior is affected by the characteristics of both molecule and membrane surface.

Hosted file

image3.emf available at <https://authorea.com/users/510119/articles/587306-molecular-dissolution-behaviors-on-porous-membrane-surface-using-hierarchical-metal-organic-framework-lamellar-membrane>

Figure 2. The solvent permeance of (a) MOF-CH₃@BDC, (b) MOF-CH₃@CH₃ and (c) MOF-CH₃@NH₂ membranes.

3.3 Dissolution activation energy

To intuitively characterize the tendency of molecules dissolving into pore entrances on membrane surface, dissolution activation energy (E_s) is proposed here, which reflects the origin and energy variation of dissolution behaviors. For molecule transport through a membrane, the total activation energy (E_p) includes E_s and diffusion activation energy (E_μ).^[48,49] The E_p is extracted from Arrhenius plot by measuring molecule permeance through membrane over a temperature range of 10 to 45 °C (Figure 3a), and the corresponding equation is:^[19,50]

$$P = P_0 \times e^{-\frac{E_p}{RT}} \quad (3)$$

In equation 3, P and P_0 (L m⁻² h⁻¹ bar⁻¹) represent the permeance of a solvent and the pre-exponential factor, respectively, R (kJ mol⁻¹ K⁻¹) is the gas constant, and T (K) is the temperature. Accordingly, E_p values of various solvents for these membranes are obtained (Tables S1 and S2). Then the E_μ is calculated by the following equations:^[51]

$$\mu = \mu_0 \times e^{\frac{E_\mu}{RT}} \quad (4)$$

In equation 4, μ and μ_0 (Pa s) are the viscosity of solvent and pre-exponential factor, respectively. By combining equations 3 and 4, the obtained expression is below:^[52]

$$P \sim \mu \times e^{-\frac{E_p}{E_\mu}} \quad (5)$$

Therefore, E_μ is obtained from the slope value in the correlation plot between solvent permeance and viscosity (Figure 3b). As an example, the E_μ of water for MOF-CH₃@CH₃ membrane is calculated to be 16.64 kJ mol⁻¹. To vouch for the accuracy of calculated E_μ values, another method based on Darcy's law is adopted (Figure S18).^[45,53] And the result is 16.96 kJ mol⁻¹, close to that calculated by equation 5. Next, E_s values of solvents for hierarchical lamellar membranes are acquired.

Note that molecules would spread on the membrane surface firstly before dissolving into membrane, where the spreading activation energy should be considered. Here, the spreading activation energy of water on MOF-CH₃@CH₃ and MOF-CH₃@NH₂ membrane surface was calculated as an example (Figures S19-22). Results show that the spreading activation energy values are comparable for MOF-CH₃@CH₃ (107.6 kJ mol⁻¹) and MOF-CH₃@NH₂ (113.2 kJ mol⁻¹) membranes, which should be resulted from the uniform MOF skeleton structure on membrane surface.^[54] To eliminate the impact of spreading activation energy value on the calculation of E_s for molecules drilling into pore entrance, membranes are immersed into corresponding solvents to reach a saturation condition, under which the following E_s values are acquired.^[55]

For molecules drilling into pore entrances, the E_s is mainly controlled by molecule-molecule and molecule-pore interactions. Specifically, molecules in bulk state need to adjust the configuration to drill into confined pores (from larger aggregates to smaller ones), during which the bindings between molecules should be broken, thus inevitably consuming energy. Meanwhile, molecules that contact the pore entrances would exert interactions with the groups on pore rims, which releases energy to compensate the energy consumed.^[56] Therefore, these two energies should determine molecular dissolution efficiency collectively. Figure 3c displays that for MOF-CH₃@CH₃ membrane with hydrophobic pores on surface layer, the E_s values of both polar

and nonpolar solvents are above 0. This indicates that the energy released by the formation of molecule-pore interactions is smaller than the energy consumed by molecule rearrangement. Thus extra energy is needed to push the molecules to drill into pore entrances. In contrast, for MOF-CH₃@NH₂ membrane with hydrophilic pores on surface layer, the E_S values for nonpolar solvents are above 0, while that for polar solvents are below 0. This finding implies that hydrophilic groups on pore entrance tend to exert stronger interactions with polar solvent (*e.g.* hydrogen bond interaction), thus producing more positive energy that compensates the energy consumed by molecule rearrangement. Therefore, polar solvents tend to spontaneously drill into hydrophilic pores. As shown in Figure 3d, taking water as an example, water molecules in bulk state are bonded with each other through hydrogen bonds. Upon contacting pore entrances, new hydrogen bonds are formed between water molecules and -NH₂ groups on pore rims. Meanwhile, the configuration of bulk water is adjusted to drill into confined pores, accompanied by the breakage of intermolecular hydrogen bonds. In this manner, water molecules dissolve into the hierarchical MOF lamellar membrane.

Hosted file

image4.emf available at <https://authorea.com/users/510119/articles/587306-molecular-dissolution-behaviors-on-porous-membrane-surface-using-hierarchical-metal-organic-framework-lamellar-membrane>

Figure 3. Correlations between water permeance and (a) temperature, (b) viscosity for MOF-CH₃@NH₂ and MOF-CH₃@CH₃ membranes. (c) The dissolution activation energy of various solvents for MOF-CH₃@NH₂ and MOF-CH₃@CH₃ membranes. (d) Schematic illustration of water molecules dissolution behavior through pores on MOF-CH₃@NH₂ membrane surface.

To support above findings, molecular dynamics (MD) simulations were performed to probe the interaction energy of molecule-molecule and molecule-pore on molecule level. Specifically, they are calculated by Lennard-Jones interaction simulation (Figures 4d, e and Table S3). Results in Figures 4a and b show that the experimentally calculated E_S values exhibit a linear relationship with that of simulated theoretical values (E_T , kJ mol⁻¹). Here, the E_T value is acquired by subtracting molecule-molecule interaction energy from molecule-pore interaction energy, which represents the theoretical dissolution activation energy. E_S and E_T obey the equation of $E_S = KE_T + C$, where K is a proportionality constant. K value should vary with properties of membrane surface property and temperature, while C is determined by the physical factors of pore, *e.g.* , steric hindrance.^[12] This equation further underpins that molecular dissolution behaviors are controlled by both molecule-molecule and molecule-pore interactions. It should be noted that some researchers calculated the interfacial resistance of molecule transporting through membrane to analysis molecule dissolution, while the resistance equation can not reveal the molecular dissolution capacity on molecule level.^[57,58]

Hosted file

image5.emf available at <https://authorea.com/users/510119/articles/587306-molecular-dissolution-behaviors-on-porous-membrane-surface-using-hierarchical-metal-organic-framework-lamellar-membrane>

Figure 4. Correlation between experimental and theoretical dissolution activation energy values of (a) MOF-CH₃@CH₃ and (b) MOF-CH₃@NH₂ membranes. (c) E_S of glucose solution, water and urea solution for MOF-CH₃@CH₃ and MOF-CH₃@NH₂ membranes. (d) Interaction energy between toluene and NH₂-BDC, toluene, CH₃-BDC. (e) Interaction energy between water and NH₂-BDC, water, CH₃-BDC. Grey for C, blue for N, red for O, white for H.

To further verify this hypothesis, molecule-molecule and molecule-pore interactions were respectively adjusted. Taking water as an example, glucose and urea solution (150 mmol L⁻¹) were mixed with water to strengthen and weak the interactions between water molecules, respectively.^[19,59] Figure 4c shows that E_S of glucose solution (24.23 kJ mol⁻¹) is higher than that of pure water (18.74 kJ mol⁻¹), suggesting that

the enhancement of water-water interactions elevates the energy for breaking hydrogen bonds from bulk state, thus lifting the E_s of water. In contrast, urea solution displays weaker water-water interactions than pure water, thus the energy for molecule arrangement is reduced and brings lower E_s (15.99 kJ mol⁻¹). For another, molecule-pore interactions were also adjusted. For instance, Figure 3c reveals that MOF-CH₃@NH₂ membrane surface with -NH₂ groups on pore entrances gives much lower E_s (-4.16 kJ mol⁻¹) for water than that of MOF-CH₃@CH₃ membrane surface with -CH₃ groups (13.70 kJ mol⁻¹). Moreover, compared with other nonpolar solvents, toluene and cyclohexane display much lower E_s for MOF-CH₃@NH₂ membrane than that of MOF-CH₃@CH₃ membrane. This is due to the weak hydrogen bonds between -NH₂ with active -H on cyclic hydrocarbon,^[60,61] which compensates for the consumed energy considerably. This again delivers the fact that molecule-pore interactions exert paramount impact on molecular dissolution behaviors.

3.4 Dissolution model equation

To further quantize the key parameters that affect molecular dissolution behaviors, the critical surface tension (γ_C) of membrane is extracted by Zisman Plot.^[57,62,63] Here, contact angles for polar (water, methanol, ethanol, acetone, acetonitrile and DMF) and nonpolar solvents (cyclohexane, n-octane, toluene, n-hexane) were measured to determine the γ_C of membranes. Zisman Plots in Figures 5a and b show that γ_C values of MOF-CH₃@NH₂ and MOF-CH₃@CH₃ membranes are 19.7 and 17.6 mN m⁻¹, respectively. This defines the wetting threshold for these two membranes, which means that solvents with surface tensions less than the γ_C are predicted to wet the membrane surface completely. Here, two phenomenological model equations that well correlate to E_s and intrinsic parameters of membrane surface and molecule are proposed for MOF-CH₃@CH₃ (equation 6) and MOF-CH₃@NH₂ (equation 7), respectively:

$$E_s = K_m \ln [(\gamma_L - \gamma_C) \mu d^2] \quad (6)$$

$$E_s = K_a \ln [(\gamma_L - \gamma_C) \delta_e \mu d^2] \quad (7)$$

where γ_L and γ_C (mN m⁻¹) are the surface tension of solvent and the critical surface tension of membrane surface, respectively, d (m) is the kinetic diameter and δ_e (Pa^{0.5}) is the Hansen solubility parameter of solvent, K_m and K_a are the coefficient constant of MOF-CH₃@CH₃ and MOF-CH₃@NH₂ membranes, respectively.

These two equations indicate that molecular dissolution capacity is positively correlated with the difference between solvent surface tension and membrane critical surface tension. Therefore, the interfacial properties ($\gamma_L - \gamma_C$) of membrane surface and molecule both count significantly in the equation. Besides, the parameters that correlate with molecule transport in pores (μd^2) also affect molecular dissolution efficiency (Figure 5c). Interestingly, molecular dissolution behaviors on MOF-CH₃@NH₂ membrane do not obey this dissolution model equation, but adding another parameter of δ_e , which represents the cohesive energy density of molecules (Figures 5d and S23). This should be ascribed to the formation of strong molecule-pore interactions, which promote the breakage of molecule-molecule interactions and then the thorough rearrangement of molecules, thus doubling the effect of molecule-molecule interaction on dissolution efficiency. According to the dissolution equations, molecular dissolution process should include two main steps: wetting the membrane surface and then entering into pores. Concretely, the wetting step is controlled by the difference of surface tension between molecule and membrane surface ($\gamma_L - \gamma_C$), which reflects the wettability of membrane surface for molecules. Subsequently, the step of molecules entering into pores should relate to the μ and d for hydrophobic pore entrances, while relating to δ_e , μ and d for hydrophilic pore entrances (Table S4). Different from the strategy of calculating interfacial resistance, this viewpoint of dissolution activation energy systematically reveals the influence of molecule-molecule and molecule-pore interactions on dissolution behaviors on molecule-level.^[12,57,58]

Hosted file

image6.emf available at <https://authorea.com/users/510119/articles/587306-molecular-dissolution-behaviors-on-porous-membrane-surface-using-hierarchical-metal-organic->

framework-lamellar-membrane

Figure 5. Zisman plots with identified critical surface tension for (a) MOF-CH₃@CH₃ and (b) MOF-CH₃@NH₂ membranes. The molecular dissolution equations of (c) MOF-CH₃@CH₃ and (d) MOF-CH₃@NH₂ membranes.

3.5 Dye rejection and stability of hierarchical MOF lamellar membranes

Then, the structural stability and long-term operational stability of as-prepared hierarchical MOF lamellar membranes were conducted. Figure 6 shows that these membranes display favorable anti-fouling and anti-pressure performance. Preliminarily, five dyes with a series of sizes were filtered through the membranes to detect rejection ability (Figures 6a and S24). Before testing, membranes were compacted under 1 bar for 20 min to reach a complete equilibrium state. MOF-CH₃@NH₂ and MOF-CH₃@CH₃ membranes exhibit comparable dye rejection, because of their similar pore sizes. Specifically, for MB with small size of 1.4 × 0.58 nm, membranes show an invalid rejection (22%). Upon increasing the size of dyes to 1.6 × 1.4 nm (RR) and 2.2 × 1.7 nm (BB), membrane rejection experiences a sharp rise to almost 100%, verifying the precise sieving of membranes by intrinsic pores (1.02 nm). Meanwhile, to detect the dye adsorption on membrane rejection, PEGs with different molecular weight were filtered through the MOF membranes, and these membranes exhibited a *MWCO* of ~600 Da (Figure S25). According to Stokes equation,^[64] the diameter is calculated to be 1.1 nm, which is well consistent with the pore size of membranes. This confirms that the dyes should be slightly adsorbed on membrane, which contribute to a higher rejection, while the size sieving effect is the main separation mechanism for these MOF membranes. In addition, cyclic operation (24 h) test displays that methanol permeance begins reducing at 16 h, and after washing, the permeance returns by 99% (Figure 6b and S26). This is ascribed to the dye molecules retained on the membrane surface block the transport of solvents to a certain extent, and after washing, the clean membrane regain its excellent performance. Moreover, pressure cyclic measurement results (Figure 6c) reveal that the lamellar structure of MOF membrane is able to bear transmembrane pressure as high as 6 bar without obvious collapse. This is supported by the negligible permeance fluctuation (below 5%) for methanol when elevating the pressure from 1 bar to 6 bar and adjusting back to 1 bar. Furthermore, long-term operation stability test (Figure 6d) displays that methanol permeance of MOF lamellar membranes experiences a moderate decline (below 5%) in the initial 2 h, and then maintains steady during the following 98 h. The slight decrease should be stemmed from the moderate compaction of adjacent nanosheets within lamellar structure, and similar observations are also reported for other lamellar membranes.^[9,43] In general, the as-prepared MOF lamellar membranes exhibit satisfactory structural and operational stability, which is mainly contributed by the strong π - π stacking interactions within membrane structure,^[65,66] holding promise for practical applications (Figure S27).

Hosted file

image7.emf available at <https://authorea.com/users/510119/articles/587306-molecular-dissolution-behaviors-on-porous-membrane-surface-using-hierarchical-metal-organic-framework-lamellar-membrane>

Figure 6. (a) Dye rejection, (b) cyclic operation measurement, (c) pressure cyclic measurement, and (d) methanol permeance and RR rejection against operation time for MOF-CH₃@NH₂ and MOF-CH₃@CH₃ membranes.

4 CONCLUSIONS

In summary, hierarchical MOF lamellar membranes with ultrathin surface layer (~7 nm) and low-resistance support layer (553 nm) were prepared by double-needled electrostatic atomization technology. The wettability of pore entrances on surface layer is subtly adjusted by hydrophilic (-NH₂) and hydrophobic (-CH₃) groups. While the inner pores with -CH₃ groups provide identical and low-resistance diffusion paths in support layer. Based on this novel platform, the underlying molecule dissolution behaviors are systematically investigated from the viewpoint of dissolution activation energy (E_s). we demonstrate that molecule-pore

and molecule-molecule interactions play crucial roles for dissolution process. For hydrophobic membrane surface, E_s is above 0 for both polar and nonpolar solvents, confirming the negative tendency for molecules to dissolve into pore entrances. In contrast, for hydrophilic membrane surface, E_s is above 0 for nonpolar solvents but below 0 for polar solvents, suggesting that polar solvents can actively dissolve into pore entrances. This is ascribed to the hydrophilic groups exert strong interactions with polar solvents, thus compensating the energy consumed by molecule rearrangement, thus permitting fast permeation (over $270 \text{ L m}^{-2} \text{ h}^{-1} \text{ bar}^{-1}$ for acetone). Significantly, dissolution model equations on hydrophilic and hydrophobic membrane surface are established, respectively, which are stemmed from the intrinsic parameters of molecules ($\mu, \delta_e, \gamma_L, d$) and membrane surface (γ_C). This elucidating molecular dissolution behaviors on porous membrane surface would provide new guidelines for the design of advanced membranes.

ACKNOWLEDGEMENTS

The authors would like to acknowledge the financial support from National Natural Science Foundation of China (U2004199), Excellent Youth Foundation of Henan Province (202300410373) and China Postdoctoral Science Foundation (2022TQ0292). Center for advanced analysis and computational science, Zhengzhou University is also highly acknowledged.

DATA AVAILABILITY STATEMENT

The data that support the findings of this study are available from the corresponding author upon reasonable request.

AUTHOR CONTRIBUTIONS

Yihao Chen: Data curation; investigation; writing-original draft; writing-review & editing. **Jingjing Chen:** Software; writing-original draft. **Chongchong Chen:** Data curation; investigation; software; writing-original draft. **Xiaoli Wu:** Funding acquisition; Software; writing-review & editing; investigation; Project administration; supervision. **Yifan Li:** Writing-original draft; supervision. **Jie Zhang:** Data curation; investigation. **Jingtao Wang:** Funding acquisition; project administration; supervision; writing-original draft; writing-review & editing.

REFERENCES

1. Brennecke JF, Freeman B. Reimagining petroleum refining. *Science* . 2020; 369:254–255.
2. Werber JR, Osuji CO, Elimelech M. Materials for next-generation desalination and water purification membranes. *Nat. Rev. Mater.* 2016;1:16018.
3. Ghalei B, Sakurai K, Kinoshita Y, Wakimoto K, Isfahani AP, Song Q, Doitomi K, Furukawa S, Hirao H, Kusuda H, Kitagawa S, Sivaniah E. Enhanced selectivity in mixed matrix membranes for CO_2 capture through efficient dispersion of amine-functionalized MOF nanoparticles. *Nat. Energy* . 2017;2:17086.
4. Freger V. Outperforming nature’s membranes. *Science* . 2015;348:1317–1318.
5. Zhang S, Li H, Li H, Sengupta B, Zha S, Li S, Yu M. Negative charge confined amine carriers within the nanowire network for stable and efficient membrane carbon capture. *Adv. Funct. Mater.* 2020;30:2002804.
6. Liu Q, Babu DJ, Hao J, Vahdat MT, Campi D, Agrawal KV. Metal soap membranes for gas separation. *Adv. Funct. Mater.* 2021;31:2005629.
7. Ding L, Wei Y, Li L, Zhang T, Wang H, Xue J, Ding LX, Wang S, Caro J, Gogotsi Y. MXene molecular sieving membranes for highly efficient gas separation. *Nat. Commun.* 2018;9:155.
8. Liu G, Jin W, Xu N. Two-dimensional-material membranes: a new family of high-performance separation membranes. *Angew. Chem., Int. Ed.* 2016;55:13384–13397.
9. Chen J, Wu X, Chen C, Chen Y, Li W, Wang J. Secondary-assembled defect-free MOF membrane *via* triple-needle electrostatic atomization for highly stable and selective organics permeation. *J. Membr. Sci.*

2022;648:120382.

10. Hu J, Yuan C, Zhi L, Zhang H, Yuan Z, Li X. In situ defect-free vertically aligned layered double hydroxide composite membrane for high areal capacity and long-cycle zinc-based flow battery. *Adv. Funct. Mater.* 2021;31:2102167.
11. Yang J, Li HN, Zhang X, Zhu CY, Yu HH, Xu ZK. Janus membranes for fast-mass-transfer separation of viscous ionic liquids from emulsions. *J. Membr. Sci.* 2021;637:119643.
12. Zhang X, Zhou W, Xu F, Wei M, Wang Y. Resistance of water transport in carbon nanotube membranes. *Nanoscale* . 2018;10:13242-13249.
13. Song Y, Wei M, Xu F, Wang Y. Molecular simulations of water transport resistance in polyamide RO membranes: interfacial and interior contributions. *Engineering* . 2020;6:577-584.
14. Uragami T, Yono T, Sugihara M, Studies on syntheses and permeabilities of special polymer membranes. 36. Permeabilities of alcohols and hydrocarbons through acrylonitrile-butadiene-styrene terpolymer membranes. *Die Angew. Makromol. Chemie* . 1979;82:89-102.
15. Sandru M, Sandru EM, Ingram WF, Deng J, Stenstad PM, Deng L, Spontak RJ. An integrated materials approach to ultrapermeable and ultraselective CO₂ polymer membranes. *Science* . 2022;376:90-94.
16. Qian Y, Shang J, Liu D, Yang G, Wang X, Chen C, Kou L, Lei W. Enhanced ion sieving of graphene oxide membranes *via* surface amine functionalization. *J. Am. Chem. Soc.* 2021;143:5080-5090.
17. Huang K, Liu G, Shen J, Chu Z, Zhou H, Gu X, Jin W, Xu N. High-efficiency water-transport channels using the synergistic effect of a hydrophilic polymer and graphene oxide laminates. *Adv. Funct. Mater.* 2015;25:5809-5815.
18. Zhang Z, Wu H, Li Y, Liu Y, Cao C, Wang H, Wang M, Pan F, Jiang Z. Heterostructured graphene oxide membranes with tunable water-capture coatings for highly selective water permeation. *J. Mater. Chem. A* . 2021;9:7903–7912.
19. Tunuguntla RH, Henley RY, Yao YC, Pham TA, Wanunu M, Noy A. Enhanced water permeability and tunable ion selectivity in subnanometer carbon nanotube porins. *Science* . 2017;357:792–796.
20. Cheng C, Iyengar SA, Karnik R. Molecular size-dependent subcontinuum solvent permeation and ultrafast nanofiltration across nanoporous graphene membranes *Nat. Nanotechnol.* 2021;16:989–995.
21. Jang D, Idrobo JC, Laoui T, Karnik R. Water and solute transport governed by tunable pore size distributions in nanoporous graphene membranes. *ACS Nano* . 2017;11:10042–10052.
22. Wan J, Huang L, Wu J, Xiong L, Hu Z, Yu H, Li T, Zhou J. Microwave combustion for rapidly synthesizing pore-size-controllable porous graphene. *Adv. Funct. Mater.* 2018;28:1800382.
23. Sapkota B, Liang W, Mohammadi AV, Karnik R, Noy A, Wanunu M. High permeability sub-nanometre sieve composite MoS₂ membranes. *Nat. Commun.* 2020;11:2747.
24. Kang J, Choi Y, Kim JH, Choi E, Choi SE, Kwon O, Kim DW. Functionalized nanoporous graphene membrane with ultrafast and stable nanofiltration. *J. Membr. Sci.* 2021;618:118635.
25. Zhang C, Wu BH, Ma MQ, Wang Z, Xu ZK. Ultrathin metal/covalent-organic framework membranes towards ultimate separation. *Chem. Soc. Rev.* 2019;48:3811–3841.
26. Wang Y, Jin H, Ma Q, Mo K, Mao H, Feldhoff A, Cao X, Li Y, Pan F, Jiang Z. A MOF glass membrane for gas separation. *Angew. Chem., Int. Ed.* 2020;59:4365–4369.
27. Liu TY, Yuan HG, Liu YY, Ren D, Su YC, Wang X. Metal-organic framework nanocomposite thin films with interfacial bindings and self-standing robustness for high water flux and enhanced ion selectivity. *ACS Nano* . 2018;12:9253–9265.

28. Dou H, Xu M, Wang B, Zhang Z, Wen G, Zheng Y, Luo D, Zhao L, Yu A, Zhang L, Jiang Z, Chen Z. Microporous framework membranes for precise molecule/ion separations. *Chem. Soc. Rev.* 2021;50:986–1029.
29. Mandal S, Natarajan S, Mani P, Pankajakshan A. Post-synthetic modification of metal-organic frameworks toward applications. *Adv. Funct. Mater.* 2021;31:2006291.
30. Feng L, Wang KY, Lv XL, Yan TH, Zhou HC. Hierarchically porous metal-organic frameworks: synthetic strategies and applications. *Natl. Sci. Rev.* 2020;7:1743–1758.
31. Lin RB, Xiang S, Zhou W, Chen B. Microporous metal-organic framework materials for gas separation. *Chem.* 2020;6:337–363.
32. Ji Z, Wang H, Canossa S, Wuttke S, Yaghi OM. Pore chemistry of metal-organic frameworks. *Adv. Funct. Mater.* 2020;30:2000238.
33. Peng Y, Li Y, Ban Y, Yang W. Two-dimensional metal-organic framework nanosheets for membrane-based gas separation. *Angew. Chem., Int. Ed.* 2017;56:9757–9761.
34. Jian M, Qiu R, Xia Y, Lu J, Chen Y, Gu Q, Liu R, Hu C, Qu J, Wang H, Zhang X. Ultrathin water-stable metal-organic framework membranes for ion separation. *Sci. Adv.* 2020;6:eaay3998.
35. Chowdhury MR, Steffes J, Huey BD, McCutcheon JR. 3D printed polyamide membranes for desalination. *Science.* 2018;361:682–686.
36. Wang Q, Wu X, Chen J, Li W, Zhang H, Wang J. Ultrathin and stable organic-inorganic lamellar composite membrane for high-performance organic solvent nanofiltration. *Chem. Eng. Sci.* 2020;228:116002.
37. Zhao S, Wang Y, Dong J, He CT, Yin H, An P, Zhao K, Zhang X, Gao C, Zhang L, Lv J, Wang J, Zhang J, Khattak AM, Khan NA, Wei Z, Zhang J, Liu S, Zhao H, Tang Z. Ultrathin metal-organic framework nanosheets for electrocatalytic oxygen evolution. *Nat. Energy.* 2016;1:16184.
38. Wang B, Zhao M, Li L, Huang Y, Zhang X, Guo C, Zhang Z, Cheng H, Liu W, Shang J, Jin J, Sun X, Liu J, Zhang H. Ultra-thin metal-organic framework nanoribbons. *Natl. Sci. Rev.* 2020;7:46–52.
39. Wang B, Shang J, Guo C, Zhang J, Zhu F, Han A, Liu J. A general method to ultrathin bimetal-MOF nanosheets arrays *via* in situ transformation of layered double hydroxides arrays. *Small.* 2019;15:1804761.
40. Wang Z, Yu Q, Huang Y, An H, Zhao Y, Feng Y, Li X, Shi X, Liang J, Pan F, Cheng P, Chen Y, Ma S, Zhang Z. PolyCOFs: a new class of freestanding responsive covalent organic framework membranes with high mechanical performance. *ACS Cent. Sci.* 2019;5:1352–1359.
41. Gonzalez-Nelson A, Mula S, Šimėnas M, Nas SB, Altenhof AR, Vojvodin CS, Canossa S, Banys JR, Schurko RW, Coudert FX, Veen MA. Emergence of coupled rotor dynamics in metal-organic frameworks *via* tuned steric interactions. *J. Am. Chem. Soc.* 2021;143:12053–12062.
42. Oveisia M, Asli MA, Mahmoodi NM. MIL-Ti metal-organic frameworks (MOFs) nanomaterials as superior adsorbents: synthesis and ultrasound-aided dye adsorption from multicomponent wastewater systems. *J. Hazard. Mater.* 2018;347:123–140.
43. Wang J, Yuan Z, Wu X, Li Y, Chen J, Jiang Z. Beetle-inspired assembly of heterostructured lamellar membranes with polymer cluster-patterned surface for enhanced molecular permeation. *Adv. Funct. Mater.* 2019;29:1900819.
44. Ding Li, Wei Y, Li L, Zhang T, Wang H, Xue J, Ding LX, Wang S, Caro J, Gogotsi Y. MXene molecular sieving membranes for highly efficient gas separation. *Nat. Commun.* 2018;9:155.
45. Boateng LK, Madarshahian R, Yoon Y, Caicedo JM, Flora JRV. A probabilistic approach for estimating water permeability in pressure-driven membranes. *J. Mol. Model.* 2016;22:185.

46. Karan S, Jiang Z, Livingston AG. Sub-10 nm polyamide nanofilms with ultrafast solvent transport for molecular separation. *Science* . 2015;348:1347–1351
47. Ruijter MJ, Coninck JD, Blake TD, Clarke A, Rankin A. Contact angle relaxation during the spreading of partially wetting drops. *Langmuir* . 1997;13:7293–7298.
48. Feng X, Huang RYM. Estimation of activation energy for permeation in pervaporation processes. *J. Membr. Sci.* 1996;118:127–131.
49. Urugami T, Maekawa K, Sugihara M. Studies on syntheses and permeabilities of special polymer membranes. 21. Permeabilities of alcohols and hydrocarbons through nylon 12 membranes. *Die Angew. Makromol. Chemie* 1980;87:175-193.
50. Chen C, Wang J, Liu D, Yang C, Liu Y, Ruoff RS, Lei W. Functionalized boron nitride membranes with ultrafast solvent transport performance for molecular separation. *Nat. Commun.* 2018;9:1902.
51. Machado DR, Hasson D, Semiat R. Effect of solvent properties on permeate flow through nanofiltration membranes. Part I: Investigation of parameters affecting solvent flux. *J. Membr. Sci.* 1999;163:93–102.
52. Urugami T, Fujimoto M, Sugihara M. Studies on syntheses and permeabilities of special polymer membranes: 24. Permeation characteristics of poly(vinylidene fluoride) membranes. *Polymer* . 1980;21:1047–1051.
53. Nair RR, Wu HA, Jayaram PN, Grigorieva IV, Geim AK. Unimpeded permeation of water through helium-leak-tight graphene-based membranes. *Science* . 2012;335:442–444.
54. Fu W, Hu SP, Song XG, Li JX, Cao J, Feng JC, Wang GD. Wettability and bonding of graphite by $\text{Sn}_{0.3}\text{Ag}_{0.7}\text{Cu-Ti}$ alloys. *Carbon N. Y.* 2017;121:536–543.
55. Starov VM, Zhdanov SA, Kosvintsev SR, Sobolev VD, Velarde MG. Spreading of liquid drops over porous substrates. *Adv. Colloid Interface Sci.* 2003;104:123–158.
56. Xu F, Dai L, Wu Y, Xu Z. $\text{Li}^+/\text{Mg}^{2+}$ separation by membrane separation: the role of the compensatory effect. *J. Membr. Sci.* 2021;636:119542.
57. Machado DR, Hasson D, Semiat R. Effect of solvent properties on permeate flow through nanofiltration membranes: Part II. Transport model. *J. Membr. Sci.* 2000;166:63–69.
58. Shevate R, Shaffer DL. Large-area 2D covalent organic framework membranes with tunable single-digit nanopores for predictable mass transport. *ACS Nano* 2022;16:2407–2418.
59. Uedaira H, Uedaira H, Role of hydration of polyhydroxy compounds in biological systems. *Cell. Mol. Biol.* 2001;47:823–829.
60. Zhang X, Shi X, Zhao Q, Li Y, Wang J, Yang Y, Bi F, Xu J, Liu N. Defects controlled by acid-modulators and water molecules enabled UiO-67 for exceptional toluene uptakes: An experimental and theoretical study. *Chem. Eng. J.* 2022;427:131573.
61. Emamian S, Lu T, Kruse H, Emamian H. Exploring nature and predicting strength of hydrogen bonds: a correlation analysis between atoms-in-molecules descriptors, binding energies, and energy components of symmetry-adapted perturbation theory. *J. Comput. Chem.* 2019;40:2868–2881.
62. Kujawa J, Kujawski W, Cerneaux S, Li G, Al-Gharabli S. Zirconium dioxide membranes decorated by silanes based-modifiers for membrane distillation-material chemistry approach. *J. Membr. Sci.* 2020;596:117597.
63. Rezayi T, Entezari MH, Moosavi F. The variation of surface free energy of Al during superhydrophobicity processing. *Chem. Eng. J.* 2017;322:181–187.

64. KongX, ZhouMY, Lin CE, Wang J, Zhao B, Wei XZ, Zhu BK. Polyamide/PVC based composite hollow fiber nanofiltration membranes: Effect of substrate on properties and performance. *J. Membr. Sci.*2016;505:231–240.
65. Alemayehu HG, Liu C, Hou J, Yang J, Fang M, Tang Z, Li L. Highly stable membrane comprising MOF nanosheets and graphene oxide for ultra-permeable nanofiltration. *J. Membr. Sci.* 2022;652:120479.
66. Li Y, Zhang X, Yang A, Jiang C, Zhang G, Mao J, Meng Q. Polyphenol etched ZIF-8 modified graphene oxide nanofiltration membrane for efficient removal of salts and organic molecules. *J. Membr. Sci.*2021;635:119521.